DROP: Dexterous Reorientation via Online Planning

Albert H. Li[†], **Preston Culbertson**[‡], **Vince Kurtz**[‡], **and Aaron D. Ames**[†,‡]
† Department of Computing and Mathematical Sciences
‡ Department of Mechanical and Civil Engineering
California Institute of Technology
{alberthli, pculbert, vkurtz, ames}@caltech.edu

Abstract: Achieving human-like dexterity is a longstanding challenge in robotics, in part due to the complexity of planning and control for contact-rich systems. In reinforcement learning (RL), one popular approach has been to use massively-parallelized, domain-randomized simulations to learn a policy *offline* over a vast array of contact conditions, allowing robust sim-to-real transfer. Inspired by recent advances in real-time parallel simulation, this work considers instead the viability of *online planning* methods for contact-rich manipulation by studying the well-known in-hand cube reorientation task. We propose a simple architecture that employs a sampling-based predictive controller and vision-based pose estimator to search for contact-rich control actions online. We conduct thorough experiments to assess the real-world performance of our method, architectural design choices, and key factors for robustness, demonstrating that our simple sampling-based approach achieves performance comparable to prior RL-based works. For the extended conference version of this paper, see: https://arxiv.org/abs/2409.14562.

Keywords: In-Hand Manipulation, Contact-Rich Planning, Sampling-based MPC

1 Introduction

1.1 Background

Achieving dexterity comparable to human hands has been a longstanding challenge in robotics research. While even simple robots can produce dynamic, contact-rich behavior [1, 2], general methods for achieving these behaviors are still scarce. Thus far, reinforcement learning (RL) has been the dominant paradigm for many contact-rich tasks due to its ability to generate real-world robust plans. One such well-studied task is in-hand cube reorientation, where a hand must rotate a cube to match as many consecutive goal orientations as possible. Pioneered by OpenAI [3] and further studied by [4, 5], RL policies trained with massively-parallelized, domain-randomized simulations have achieved robust sim-to-real transfer for cube rotation. But, this *offline* approach requires substantial pre-execution computation and is inflexible to changing task specifications.

Leveraging recent advances in real-time parallel simulation (e.g., MJPC) [6], we instead study the *online* approach of sampling-based predictive control (SPC) methods for in-hand manipulation, which continuously replan by simulating parallel rollouts and applying optimal control actions over short time horizons. In contrast with RL, this method can adjust the task or model without re-training, but may demand expensive online computation and simulation. While tools like MJPC have made SPC feasible for many simulated contact-rich tasks, their real-world utility remains largely unproven.

We present DROP (**D**exterous **R**eorientation via **O**nline **P**lanning), a system architecture (Fig. 1) consisting of (i) a simple sampling-based planner and (ii) a vision-based cube pose estimator. DROP is the first demonstration of an online planning method for cube reorientation on hardware (and the first model-based approach), and has performance comparable with prior RL-based methods. We provide extensive experiments and ablations to evaluate DROP's performance and architecture.

8th Conference on Robot Learning (CoRL 2024), Munich, Germany.

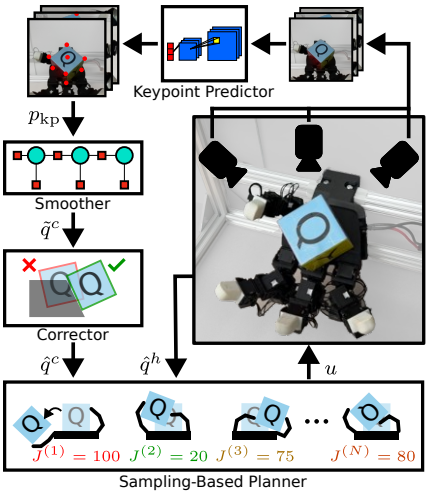

Algorithm 1: Sampling-based Predictive Control

Input: θ, N, planner-specific parameters.

while *planning* **do**

- $x_0 \leftarrow \hat{x}(t)$; `// estimate curr state`
- **for** $i = 1$ *to* N ; `// multi-threaded`
- **do**
  - $U^{(i)} \sim \pi_\theta(U)$; `// sample controls`
  - $J^{(i)} \leftarrow J\left(U^{(i)}; x_0\right)$; `// eval rollout`
- $\theta \leftarrow$ `update_params` $\left(U^{(1:N)}, J^{(1:N)}\right)$;
- $u(t) \leftarrow$ `get_action`(θ, t) ; `// async`

Figure 1: **The DROP Architecture and Algorithm.** DROP consists of (i) a vision-based cube pose estimator and (ii) a sampling-based planner that selects controls with model-based rollouts, iteratively improving the sampling distribution online. The generic sampling-based predictive control algorithm is shown to the right.

1.2 Mathematical Notation

We model the continuous-time cube-in-hand dynamics as

$$\dot{x}(t) = f\left(x(t), u(t)\right), \tag{1}$$

where x is the state and u are control inputs. We do not assume access to f except via a simulator (MuJoCo [7]) that generates state trajectories $x(t)$ given an initial state x_0 and control sequence $u(t)$.

The state x consists of the positions and velocities of both the cube (q^c, v^c) and hand (q^h, v^h):

$$x = [q, v] = [q^c, q^h, v^c, v^h]. \tag{2}$$

The controls u are position setpoints for the hand, which are tracked by a lower-level PD controller internal to the model f. We represent a control trajectory $u(t)$ on $t \in [0, T]$ with K spline knots,

$$U = [u_1, u_2, \ldots, u_k, \ldots, u_K], \tag{3}$$

which are the decision variables for online planning. The objective is encoded by a cost functional

$$J(U; x_0) = \int_0^T \ell\left(x(t), u(t)\right) dt, \tag{4}$$

where querying $J(U; x_0)$ requires simulating f using an open-loop control signal $u(t)$ from x_0.

2 The DROP Architecture

DROP consists of (i) a sampling-based planner and (ii) a keypoint-based cube pose estimator (see Fig. 1). The planner continually updates the control spline U via SPC. We use MJPC [6] to handle both parallel rollouts and policy updates. The estimator details are elided to the appendix.

Algorithm 1 describes a generic SPC procedure. At time $t \in \mathbb{R}$, the planner receives a state estimate $\hat{x}(t)$ and rolls out N open-loop control sequences $U^{(i)}$ drawn from some parametric distribution $\pi_\theta(U)$. Each trajectory is simulated (in parallel) to obtain a cost $J^{(i)}$, which are jointly used to update the sampling parameters θ. The control input $u(t)$ can be obtained for any time t from the spline parameters U, allowing asynchronous planning and θ to be updated as quickly as possible.

We test two planning strategies that both use a diagonal Gaussian distribution $\pi_\theta(U) = \mathcal{N}(\overline{U}, \Sigma)$ with $\theta = (\overline{U}, \Sigma)$. In Algorithm 1, `get_action`$(\theta, t)$ is a spline interpolation with knots $\overline{U}$.

Predictive sampling (PS) repeatedly updates $\overline{U}$ to be the best sample, fixing $\Sigma = \sigma^2 I$. Despite its simplicity, PS has demonstrated surprisingly effective performance on complex robot manipulation and locomotion tasks in simulation [6].

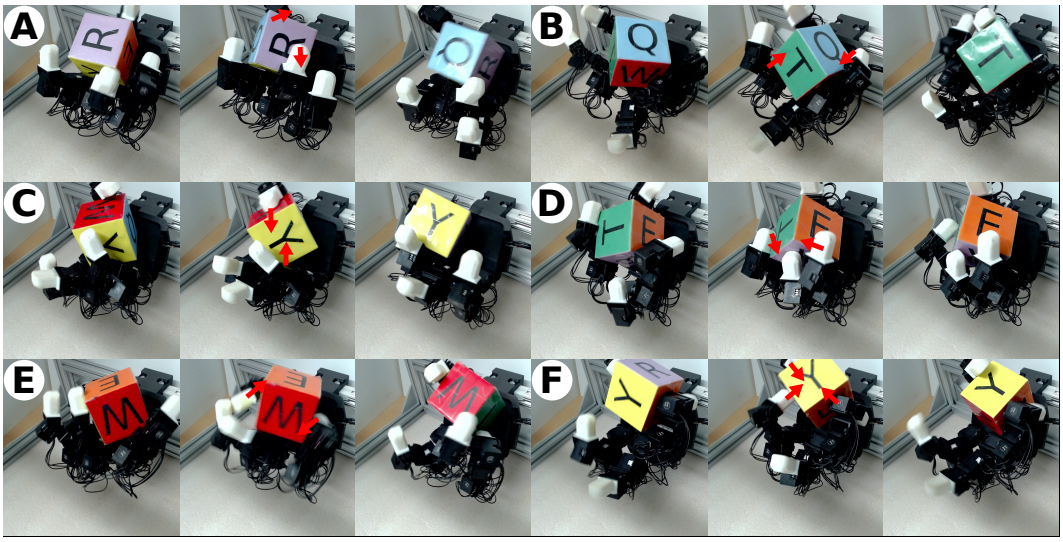

Figure 2: **Examples of rotations.** CEM can discover many contact-rich plans for cube reorientation. The red arrows show where forces are primarily applied to achieve rotations. **(A)** The middle finger pushes down on a cube edge while the base of the thumb lifts the opposite corner, rotating the Q face up. **(B)** The ring finger and base of the index finger push on opposite corners to rotate the T face up. **(C)** The thumb pulls down on the W face while the base of the ring finger pushes on the opposite corner to rotate the Y face up. **(D)** The index finger pushes down on the edge of the T face while the ring finger swipes left on the E face to rotate it up. **(E)** The ring finger first swipes inwards, then the thumb quickly follows to pull the W face up. **(F)** The thumb and the ring finger pinch and lift the cube, then the index finger pushes on an edge to rotate the Y face up. The cube is calmly lowered onto the palm.

The **cross-entropy method (CEM)** instead fits both $\bar{U}$ and $\Sigma = \text{diag}(s)$ to the sample mean and variance of the M best *elite samples*, where s is a vector of covariances. CEM is only marginally more complex than PS, but has long been used for general gradient-free optimization [8].

As in prior work [4], we use a dexterous hand to rotate a cube to within 0.4 rad of as many goal orientations in a row as possible without dropping. The goals are uniformly sampled over $SO(3)$. Unlike [4], to ensure sufficient task difficulty, each new goal must be at least 90° from the prior one.

3 Experiments

We conducted experiments to evaluate DROP's performance on hardware on the PS and CEM planners as well as the gradient-based iLQR planner. In addition to setup details, the appendix also contains ablations of various parts of the DROP architecture and simulated robustness studies.

We study each planner by running 10 trials of the cube reorientation task and analyzing the associated rotation and timing statistics. For examples of interesting rotations, see Fig. 2, and for quantitative results, see Table 1B. Following prior work, we report statistics assuming the run ends if 80s have elapsed without reaching a goal. Since this cutoff is arbitrary and we used a fairly conservative cost that slows rotation rate, we also report results for the same runs while ignoring the timeout period, ending only when the cube is dropped. For iLQR and PS, this did not change the results.

CEM greatly outperforms PS and iLQR. While iLQR is unable to achieve any rotations and PS only achieves single-digit rotations in hardware, CEM is able to achieve dozens of rotations. Moreover, the rate that it can rotate the cube is also nearly 50% faster than PS, suggesting that it can discover and/or execute contact-rich plans much more effectively.

CEM discovers nontrivial contact sequences. CEM finds contact-rich plans that leverage contacts with all parts of the hand. Many rotations are only feasible when the hand first partially rotates the cube using an initial contact sequence, then completes the rotation by gaiting the cube to a different set of contacts. For example, in Fig. 2D, the cube is first pushed forward and continually supported

	Planner	Num Rots (Sorted)	Mean Rots	Median Rots	Mean Rot/s ↑	Median Rot/s ↑
(A) Prior Work	Dactyl [3]	9, 12, 13, 19, 28, 29, 29, 32, 43, 50	26.4 ± 13.4	28.5	Not Reported	Not Reported
	Dextreme [4]	1, 6, 6, 10, 10, 18, 18, 36, 61, 112	27.8 ± 19.0	14.0	Not Reported	Not Reported
(B) Main Results	iLQR	0, 0, 0, 0, 0, 0, 0, 0, 0, 0	0 ± 0	0	N/A	N/A
	PS	0, 0, 1, 1, 1, 2, 2, 3, 4, 5	1.9 ± 1.58	1.5	0.063 ± 0.070	0.033 (0.021, 0.061)
	CEM	2, 2, 11, 11, 17, 22, 27, 34, 39, 48	21.3 ± 14.8	19.5	0.090 ± 0.081	0.062 (0.038, 0.106)
	CEM (No T/O)	2, 10, 11, 11, 22, 39, 48, 53, 59, 81	33.6 ± 24.9	30.5	0.086 ± 0.085	0.063 (0.038, 0.103)
(C) CEM Ablations (No T/O)	RGB Only	1, 1, 12, 13, 20, 37, 52, 79, 94, 128	43.7 ± 41.4	28.5	0.081 ± 0.106	0.053 (0.030, 0.089)
	No Corrector	3, 4, 6, 9, 11, 14, 17, 20, 40, 97	22.1 ± 27.0	12.5	0.065 ± 0.063	0.046 (0.029, 0.080)
	Half Rollouts	2, 7, 17, 21, 21, 27, 29, 37, 44, 65	27.0 ± 17.4	24.0	0.062 ± 0.070	0.040 (0.022, 0.072)

Table 1: **Hardware experiments.** **(A)** Prior works using RL for cube reorientation. Note that [3] performs *axis-aligned* rotations. Best results are shown. **(B)** Among online planners, CEM clearly performs the best. All planners use 120 threads, RGBD images, and the cube pose corrector. We note that when ignoring the 80s timeout imposed in [3, 4], CEM achieves higher mean and median rotation counts than Dactyl and Dextreme. **(C)** Hardware ablations show that using depth images slightly improves rotation rate, but using the corrector and as many threads as possible substantially boosts performance.

by the thumb, allowing the index and ring fingers to then swipe in opposite directions to rotate the cube. Similarly, in Fig. 2F, the thumb and ring finger pinch and lift the entire cube, which allows the index finger to rotate it about the pinched axis before the cube is safely lowered back onto the palm.

Moreover, many discovered plans exploit contact modes that are traditionally challenging to find, like sliding on edges and corners. To execute these motions, the planner employs intuitive strategies like maximizing torque by levering the cube close to a corner or edge. Lastly, our conservative cost function also induced safeguarding behavior, where fingers preemptively blocked the cube from the palm's edges or carefully supported the cube during risky rotations.

The gradient-based iLQR planner is not viable. Corroborating recent work [6, 9], we find that stiff contact dynamics prevent gradient-based methods from effectively finding good plans due to poor numerical conditioning, causing erratic behaviors that do not lead to coherent rotation sequences.

DROP performs comparably to RL. While it is challenging to compare our results to prior RL-based methods like Dactyl [3] or Dextreme [4] due to many factors distinguishing each setup, like hand morphology, cube size, physical properties, camera type, or vision model, Table 1A/B shows that our simple CEM planner approaches the performance of RL-based rotation policies (outperforming them when ignoring timeouts) with similar dexterity (see Fig. 2).

4 Conclusion and Future Directions

We present DROP, an online planning method for in-hand manipulation that achieves robust cube rotations in hardware. While promising, there are many avenues for future research.

Better planners. While we found that vanilla CEM already achieved impressive results, many more sophisticated algorithms exist, such as CMA-ES [10], MPPI [11], etc.

Robustness. DROP often plans "risky" actions, possibly due to differences between real-world and simulated physics. Incorporating domain randomization or risk-sensitivity into search-based planners, like successful RL approaches, remains an open challenge, especially due to the extra computation required to simulate randomized physics online.

Enhanced, data-driven search. As noted in our ablations, finding good plans via search demands many threads; indeed, our reported results rely on a server-grade CPU. Thus, improving efficiency is key for better performance. Promising directions include sampling from imitation-learned policies [12], learning value functions for rollout evaluation [13], and exploring alternate spline parameterizations [10] or action spaces [14]. Searching for high-level commands to provide to a lower-level RL policy could perhaps yield systems with both the flexibility of search and robustness of RL.

The simplicity of DROP opens many paths for advancing contact-rich manipulation. It is our hope that algorithms like DROP can generalize to more challenging real-world tasks than cube reorientation, permitting tool use, enhanced human-robot collaboration, and more.

References

[1] T. Ishihara, A. Namiki, M. Ishikawa, and M. Shimojo. Dynamic pen spinning using a high-speed multifingered hand with high-speed tactile sensor. In *2006 6th IEEE-RAS International Conference on Humanoid Robots*, pages 258–263, 2006. doi:10.1109/ICHR.2006.321394.

[2] N. Chavan-Dafle, A. Rodriguez, R. Paolini, B. Tang, S. Srinivasa, M. Erdmann, M. T. Mason, I. Lundberg, H. Staab, and T. Fuhlbrigge. Extrinsic dexterity: In-hand manipulation with external forces. In *Proceedings of (ICRA) International Conference on Robotics and Automation*, pages 1578 – 1585, May 2014.

[3] OpenAI, M. Andrychowicz, B. Baker, M. Chociej, R. Józefowicz, B. McGrew, J. Pachocki, A. Petron, M. Plappert, G. Powell, A. Ray, J. Schneider, S. Sidor, J. Tobin, P. Welinder, L. Weng, and W. Zaremba. Learning dexterous in-hand manipulation. *CoRR*, abs/1808.00177, 2018. URL http://arxiv.org/abs/1808.00177.

[4] A. Handa, A. Allshire, V. Makoviychuk, A. Petrenko, R. Singh, J. Liu, D. Makoviichuk, K. V. Wyk, A. Zhurkevich, B. Sundaralingam, Y. Narang, J.-F. Lafleche, D. Fox, and G. State. Dextreme: Transfer of agile in-hand manipulation from simulation to reality, 2024. URL https://arxiv.org/abs/2210.13702.

[5] T. Chen, M. Tippur, S. Wu, V. Kumar, E. Adelson, and P. Agrawal. Visual dexterity: In-hand reorientation of novel and complex object shapes. *Science Robotics*, 8(84), Nov. 2023. ISSN 2470-9476. doi:10.1126/scirobotics.adc9244. URL http://dx.doi.org/10.1126/scirobotics.adc9244.

[6] T. Howell, N. Gileadi, S. Tunyasuvunakool, K. Zakka, T. Erez, and Y. Tassa. Predictive sampling: Real-time behaviour synthesis with mujoco, 2022. URL https://arxiv.org/abs/2212.00541.

[7] E. Todorov, T. Erez, and Y. Tassa. Mujoco: A physics engine for model-based control. In *2012 IEEE/RSJ international conference on intelligent robots and systems*, pages 5026–5033. IEEE, 2012.

[8] R. Rubinstein. The cross-entropy method for combinatorial and continuous optimization, 1999.

[9] H. J. T. Suh, M. Simchowitz, K. Zhang, and R. Tedrake. Do differentiable simulators give better policy gradients?, 2022. URL https://arxiv.org/abs/2202.00817.

[10] J. Jankowski, L. Brudermüller, N. Hawes, and S. Calinon. Vp-sto: Via-point-based stochastic trajectory optimization for reactive robot behavior. In *2023 IEEE International Conference on Robotics and Automation (ICRA)*, pages 10125–10131, 2023. doi:10.1109/ICRA48891.2023.10160214.

[11] G. Williams, P. Drews, B. Goldfain, J. M. Rehg, and E. A. Theodorou. Information-theoretic model predictive control: Theory and applications to autonomous driving. *IEEE Transactions on Robotics*, 34(6):1603–1622, 2018. doi:10.1109/TRO.2018.2865891.

[12] C. Chi, Z. Xu, S. Feng, E. Cousineau, Y. Du, B. Burchfiel, R. Tedrake, and S. Song. Diffusion policy: Visuomotor policy learning via action diffusion. *The International Journal of Robotics Research*, 2024.

[13] D. Silver, A. Huang, C. J. Maddison, A. Guez, L. Sifre, G. van den Driessche, J. Schrittwieser, I. Antonoglou, V. Panneershelvam, M. Lanctot, S. Dieleman, D. Grewe, J. Nham, N. Kalchbrenner, I. Sutskever, T. Lillicrap, M. Leach, K. Kavukcuoglu, T. Graepel, and D. Hassabis. Mastering the game of go with deep neural networks and tree search. *Nature*, 529(7587):484–489, Jan. 2016. ISSN 1476-4687. doi:10.1038/nature16961. URL http://dx.doi.org/10.1038/nature16961.

[14] R. Martín-Martín, M. Lee, R. Gardner, S. Savarese, J. Bohg, and A. Garg. Variable impedance control in end-effector space. an action space for reinforcement learning in contact rich tasks. In *Proceedings of the International Conference of Intelligent Robots and Systems (IROS)*, 2019.

[15] Z.-H. Yin, B. Huang, Y. Qin, Q. Chen, and X. Wang. Rotating without seeing: Towards in-hand dexterity through touch. *Robotics: Science and Systems*, 2023.

[16] L. Röstel, J. Pitz, L. Sievers, and B. Bäuml. Estimator-coupled reinforcement learning for robust purely tactile in-hand manipulation. In *2023 IEEE-RAS 22nd International Conference on Humanoid Robots (Humanoids)*, pages 1–8. IEEE, 2023.

[17] T. Chen, J. Xu, and P. Agrawal. A system for general in-hand object re-orientation, 2021. URL https://arxiv.org/abs/2111.03043.

[18] M. Posa, C. Cantu, and R. Tedrake. A direct method for trajectory optimization of rigid bodies through contact. *The International Journal of Robotics Research*, 33:69 – 81, 2014. URL https://api.semanticscholar.org/CorpusID:6532910.

[19] N. Doshi, K. Jayaram, B. Goldberg, Z. Manchester, R. Wood, and S. Kuindersma. Contact-implicit optimization of locomotion trajectories for a quadrupedal microrobot. In *Robotics: Science and Systems XIV*, RSS2018. Robotics: Science and Systems Foundation, June 2018. doi:10.15607/rss.2018.xiv.041. URL http://dx.doi.org/10.15607/RSS.2018.XIV.041.

[20] S. L. Cleac'h, T. Howell, S. Yang, C.-Y. Lee, J. Zhang, A. Bishop, M. Schwager, and Z. Manchester. Fast contact-implicit model-predictive control, 2023. URL https://arxiv.org/abs/2107.05616.

[21] V. Kurtz, A. Castro, A. Özgün Önol, and H. Lin. Inverse dynamics trajectory optimization for contact-implicit model predictive control, 2023. URL https://arxiv.org/abs/2309.01813.

[22] A. Aydinoglu and M. Posa. Real-time multi-contact model predictive control via admm, 2022. URL https://arxiv.org/abs/2109.07076.

[23] W. Yang and M. Posa. Dynamic on-palm manipulation via controlled sliding. In *Proceedings of Robotics: Science and Systems*, July 2024.

[24] W. Yang and W. Jin. Contactsdf: Signed distance functions as multi-contact models for dexterous manipulation, 2024. URL https://arxiv.org/abs/2408.09612.

[25] C. Chen, P. Culbertson, M. Lepert, M. Schwager, and J. Bohg. Trajectotree: Trajectory optimization meets tree search for planning multi-contact dexterous manipulation. In *2021 IEEE/RSJ International Conference on Intelligent Robots and Systems (IROS)*, pages 8262–8268, 2021. doi:10.1109/IROS51168.2021.9636346.

[26] T. Pang, H. J. T. Suh, L. Yang, and R. Tedrake. Global planning for contact-rich manipulation via local smoothing of quasi-dynamic contact models, 2023. URL https://arxiv.org/abs/2206.10787.

[27] S. Lavalle and J. Kuffner. Rapidly-exploring random trees: Progress and prospects. *Algorithmic and computational robotics: New directions*, 01 2000.

[28] L. Kavraki, P. Svestka, J.-C. Latombe, and M. Overmars. Probabilistic roadmaps for path planning in high-dimensional configuration spaces. *IEEE Transactions on Robotics and Automation*, 12(4):566–580, 1996. doi:10.1109/70.508439.

[29] M. Kalakrishnan, S. Chitta, E. Theodorou, P. Pastor, and S. Schaal. Stomp: Stochastic trajectory optimization for motion planning. In *2011 IEEE International Conference on Robotics and Automation*, pages 4569–4574, 2011. doi:10.1109/ICRA.2011.5980280.

[30] C. Pezzato, C. Salmi, M. Spahn, E. Trevisan, J. Alonso-Mora, and C. H. Corbato. Sampling-based model predictive control leveraging parallelizable physics simulations, 2023.

[31] M. Bhardwaj, B. Sundaralingam, A. Mousavian, N. D. Ratliff, D. Fox, F. Ramos, and B. Boots. STORM: An integrated framework for fast joint-space model-predictive control for reactive manipulation. In *5th Annual Conference on Robot Learning*, 2021.

[32] C. Doersch, P. Luc, Y. Yang, D. Gokay, S. Koppula, A. Gupta, J. Heyward, I. Rocco, R. Goroshin, J. Carreira, and A. Zisserman. Bootstap: Bootstrapped training for tracking-any-point, 2024. URL https://arxiv.org/abs/2402.00847.

[33] N. Karaev, I. Rocco, B. Graham, N. Neverova, A. Vedaldi, and C. Rupprecht. CoTracker: It is better to track together. 2023.

[34] Y. Xiao, Q. Wang, S. Zhang, N. Xue, S. Peng, Y. Shen, and X. Zhou. Spatialtracker: Tracking any 2d pixels in 3d space. In *Proceedings of the IEEE/CVF Conference on Computer Vision and Pattern Recognition (CVPR)*, 2024.

[35] B. Wen, W. Yang, J. Kautz, and S. Birchfield. FoundationPose: Unified 6d pose estimation and tracking of novel objects. In *CVPR*, 2024.

[36] K. Greff, F. Belletti, L. Beyer, C. Doersch, Y. Du, D. Duckworth, D. J. Fleet, D. Gnanapragasam, F. Golemo, C. Herrmann, T. Kipf, A. Kundu, D. Lagun, I. Laradji, H.-T. D. Liu, H. Meyer, Y. Miao, D. Nowrouzezahrai, C. Oztireli, E. Pot, N. Radwan, D. Rebain, S. Sabour, M. S. M. Sajjadi, M. Sela, V. Sitzmann, A. Stone, D. Sun, S. Vora, Z. Wang, T. Wu, K. M. Yi, F. Zhong, and A. Tagliasacchi. Kubric: a scalable dataset generator. 2022.

[37] A. Li. Drop: Dexterous reorientation via online planning. https://caltech-amber.github.io/drop/, 2024.

[38] F. Dellaert and G. Contributors. borglab/gtsam, May 2022. URL https://github.com/borglab/gtsam).

[39] J. Abou-Chakra, K. Rana, F. Dayoub, and N. Sünderhauf. Physically embodied gaussian splatting: A realtime correctable world model for robotics, 2024. URL https://arxiv.org/abs/2406.10788.

[40] K. Shaw, A. Agarwal, and D. Pathak. Leap hand: Low-cost, efficient, and anthropomorphic hand for robot learning, 2023. URL https://arxiv.org/abs/2309.06440.

[41] W. Li and E. Todorov. Iterative linear quadratic regulator design for nonlinear biological movement systems. In *Proceedings of the First International Conference on Informatics in Control, Automation and Robotics - Volume 1: ICINCO,*, pages 222–229. INSTICC, SciTePress, 2004. ISBN 972-8865-12-0. doi:10.5220/0001143902220229.

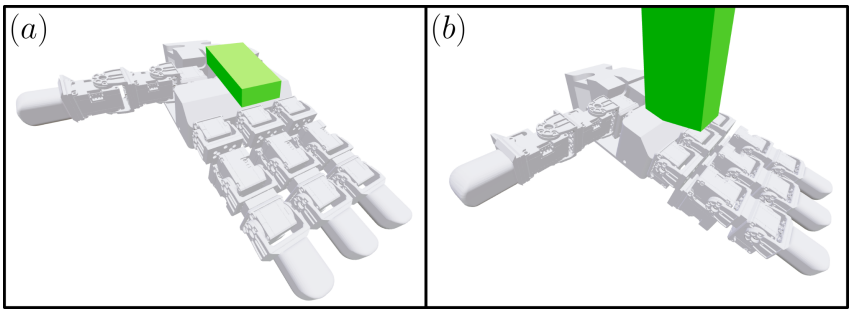

Figure 3: The safe regions $\mathcal{S}$ (green) for (a) when the cube's xy coordinates lie in the palm, and (b) when the cube's xy coordinates lie outside the palm.

Appendix

A Related Work

The first viable methods for in-hand cube reorientation employed ***reinforcement learning (RL)***, starting with Dactyl [3], which popularized domain randomization for sim-to-real transfer of RL policies. Subsequent research built on Dactyl with improved domain randomization [4], tactile-only sensing [15, 16], and "palm-down" rotations for various objects [17, 5]. While typically limited to specific robots or object classes, RL's robust hardware performance has established it as the standard for in-hand manipulation.

Others have explored model-based approaches to contact-rich manipulation via ***contact-implicit trajectory optimization*** (CITO). Originally used in locomotion [18, 19], recent work [20, 6] shows that such planners can generate motions for simple contact-rich tasks like bimanual lifting [21] or real-time planar rolling and sliding [22, 23]. Other approaches have combined CITO with learned signed distance fields [24], global search [25], or smoothed dynamics [26].

Sampling-based planning has a long history in manipulation, starting with methods like RRT, PRM, and STOMP [27, 28, 29]. Recent advances in SPC [11, 10] have enabled simple contact-rich manipulation like pushing, sliding, and pick and place [30, 31], while new tools for real-time parallel simulation of contact-rich tasks [6], have made SPC viable for simulated contact-rich tasks with remarkably simple controllers. Still, little evidence exists to show the viability of SPC for real-world contact-rich manipulation, and overall, model-based methods (like SPC or CITO) have seldom studied tasks as hard as cube reorientation, which exhibits many simultaneous unpredictable contact modes.

Lastly, high-quality ***object tracking*** is key for most of these methods, especially model-based online search. RL approaches [3, 4] usually use deep neural networks for single-object pose estimation, but recent computer vision advances suggest that more general tracking pipelines like frame-to-frame point trackers [32, 33, 34] and foundation models for rigid body pose prediction [35] may boost performance.

This appendix aims to make precise some of the technical details that were omitted from the main body of the paper for brevity.

B Sampling-based Predictive Control Implementation

Warm-starts by time shifting. Recall the generic SPC procedure described in Algorithm 1. Because the cost J at some time depends on the current state $x_0 = \hat{x}(t)$, once time elapses, the optimization problem (8) changes. Instead of solving the problem from scratch, the solution is *warm started* by applying a time shift to the previous solution (e.g., as in [**?**]). For the last time step of the warm-started solution, we simply copy the second-to-last spline parameter.

To be precise, let h denote an iteration of the mean control spline knots $\overline{U}$. Then, applying the shift operation gives

$$\overline{U}[h] = [u_1[h], u_2[h], \ldots, u_K[h]]\,,$$
$$\text{shift}\left(\overline{U}[h]\right) = [u_2[h], u_3[h], \ldots, u_K[h], u_K[h]]\,,$$

which the new samples will be centered on (and similarly for any other parameters like sampling variances).

Retaining the best rollout in PS. In predictive sampling (PS), MJPC additionally keeps the current nominal (i.e., the best) control spline as one of the samples when resampling, so that if none of the sampled trajectories improves performance, the nominal policy is not updated. We found that this is critical to the performance of PS.

Minimum standard deviation in CEM. While the sampling variance is fixed in PS, in CEM, a diagonal covariance is repeatedly fit to the top M elite samples. However, in practice, the variance may quickly collapse to very low values, preventing the planner from exploring. Therefore, we specify a minimum standard deviation uniformly over the diagonal entries of Σ, denoted σ_{min}.

Default Parameters. Table 2 lists the values of planner parameters used in experiments unless otherwise stated.

Method	Parameter	Value
All	Spline Order	0
	Plan Horizon	1.0s
	Plan Timestep	0.01s
	Num Spline Knots	4
PS	Num Samples	120
	Sampling Stdev	0.3
CEM	Num Samples	120
	Num Elites	4
iLQR	Num Parallel Line Search Threads	120

Table 2: Default planner parameter values used in all experiments.

C The Pose Estimation Pipeline

Our pose estimator consists of three parts: a keypoint predictor, a fixed-lag smoother, and a collision-aware corrector.

We use the following notation to denote "subtraction" of two quaternions $a, b \in \mathbb{H}$:

$$a \ominus b := \text{Log}\left(a \circ b^{-1}\right) \in \mathfrak{so}(3), \tag{5}$$

and similarly, when $a, b \in SE(3)$, $a \ominus b \in \mathfrak{se}(3)$.

Keypoint Prediction. The estimator takes in images $I_c \in \mathbb{R}^{C\times H\times W}$ from n_c cameras. We first train a vision model g_φ that predicts 8 fixed keypoints on the cube corresponding to its corners, $p_{\text{kp}} = g_\varphi(I_c)$. The keypoint prediction task is supervised from a training dataset of 686,000 images of a simulated cube rendered by `Blender`, which includes ground-truth pixel locations for all keypoints, even those that are outside the frame or occluded. We generate randomized background scenes using `kubric` [36], which spawns the cube along with other random assets in a `pybullet` simulation. Similar datasets are commonly used to train "track-any-point" models [32, 33, 34] which exhibit strong sim-to-real transfer for similar keypoint tracking tasks.

Crucially, we then augment these images with random affine transforms; visual effects like color, shadow, and contrast; and randomized backgrounds. We also found that pruning images where the cube was nearly occluded, or too close for a reliable pose estimate, was essential for good performance. Figure 4 shows some of the resulting images.

Figure 4: **Image augmentations.** To train the keypoint predictor, we augmented simulated images of the cube with random crops, affine transformations, spliced backgrounds, random deletions, and visual adjustments in color, contrast, brightness, and reflectivity.

To train g_φ, we fine-tuned an ImageNet-pretrained `resnet18` using `AdamW` with an MSE loss. The only model adjustments were the number of input channels (depending on RGB or RGBD inputs) and the dimension of the output layer. For finer details, see [37, Extended Version].

Pose Smoothing. We use GTSAM [38], a factor graph-based state estimation package, to convert keypoints into a cube pose estimate via fixed-lag smoothing. Given a fixed pinhole camera model with known camera poses and cube size, we derive keypoint measurement factors that relate keypoints p_{kp} to a cube pose q^c. This allows GTSAM to fuse keypoint predictions from an arbitrary number of cameras in real-time to yield a smoothed cube pose estimate $\tilde{q}^c$. See our open-source implementation for exact details [37].

In both simulation and hardware, we estimate velocities by numerically differentiating position estimates (drawn from the smoother for the cube and joint encoders for the hand) and applying an exponential moving average filter with parameter $\alpha = 0.1$ to compute a smooth velocity estimate $\tilde{v}$.

Collision-Aware Correction. While the smoother's cube pose estimate $\tilde{q}^c$ is usually accurate within 1cm, it may not always be physically compatible with the hand configuration $\tilde{q}^h$ from the encoders, as the smoother has no knowledge of collision dynamics. Thus, $\tilde{q} = [\tilde{q}^c, \tilde{q}^h]$ often corresponds to non-negligible interpenetration between cube and hand, which (i) leads to inaccurate plans that destabilize the closed-loop system, and (ii) decreases the planning rate, as stiff MuJoCo models with high interpenetration are poorly-conditioned, requiring more solver iterations.

To remedy this, we adapt the method of [39] by using a *corrector*, which maintains an asynchronous internal model

$$\dot{\hat{x}} = \hat{f}(\hat{x}(t), u(t)) \tag{6}$$

with state $\hat{x} = [\hat{q}^c, \hat{q}^h, \hat{v}^c, \hat{v}^h]$.

The corrector receives an un-adjusted estimate $\tilde{x}$ from the smoother and encoders, and computes a "corrective wrench"

$$w = -C_P(\hat{q}^c \ominus \tilde{q}^c) - C_D(\hat{v}^c - \tilde{v}^c) \tag{7}$$

that is added to (6) as a generalized force. Since the corrector starts in a feasible state, simulating (6) results in a corrected estimate $\hat{x}$ that is always physically feasible, but pulled toward the (possibly infeasible) vision-based estimate $\tilde{x}$. We also add a constant corrective force in the direction of gravity to counteract any smoother estimates that may unrealistically pull the cube upwards due to high corrector gains C_P, overwhelming the natural gravitational forces of (6).

D Specifics of the DROP Control Problem

Mathematically, the DROP cube reorientation problem is expressed as the optimal control problem

$$\begin{aligned} \min_{u} \int_0^T \left\{ \lambda_{\mathrm{g}} \cdot \ell_{\mathrm{g}}(r^c(t)) + \lambda_{\mathrm{p}} \cdot \ell_{\mathrm{p}}(p^c(t)) \right\} dt \\ \text{s.t.} \quad \dot{x}(t) = f(x(t), u(t)), \\ x(0) = x_0, \end{aligned} \tag{8}$$

where $\lambda_{(\cdot)}$ denote weights, the dynamics $f(x, u)$ are only available through simulation, and

$$\ell_{\mathrm{g}}(r^c) := \left\| r^c \ominus r^c_{\mathrm{goal}} \right\|_2^2, \tag{9}$$

$$\ell_{\mathrm{p}}(p^c) := \mathrm{dist}_{\mathcal{S}}(p^c), \tag{10}$$

are running costs. The variables p^c and r^c denote the positional and rotational components of the cube pose $q^c = [p^c, r^c]$, which are extracted from the simulated state $x(t)$. ℓ_{g} penalizes rotational distance from the goal, while ℓ_{p} penalizes the cube leaving a "safe" region $\mathcal{S}$ in Cartesian space.

In this work, we prioritize drop reduction by setting λ_{p} high and choosing a conservative region $\mathcal{S}$ (for details, see [37]). In practice, we use a relatively low λ_{g}, which slows down the planner but also amplifies differences in rotation rate across methods, allowing easier quantitative comparison.

The position cost term. We now explain the exact form of the position cost term $\ell_{\mathrm{p}}(p^c)$ in (10). The function $\mathrm{dist}_{\mathcal{S}}(\cdot)$ is parameterized by the "safe region" $\mathcal{S}$ in which we would like the cube's center to remain. Specifically, we have

$$\begin{aligned} \mathrm{dist}_{\mathcal{S}}(p^c) &:= d(\|p^c\|_{\mathcal{S}}), \\ d(x) &:= 0.05 \cdot \log\left(1 + \exp\left(\frac{250x}{0.05}\right)\right), \end{aligned} \tag{11}$$

where $\|x\|_{\mathcal{S}}$ reports the Euclidean distance between a point x and a set $\mathcal{S}$, and $d(x)$ is a scalar-valued function that applies a very quickly-growing penalty when $x > 0$. In particular, its parameters are chosen such that when $x = 0.01$, $d(x) \approx 1$.

The set $\mathcal{S}$ is defined by two cases. If the cube's x and y coordinates lie within a specified rectangle, then we parameterize $\mathcal{S}$ as a parallelepiped whose x and y faces are axis-aligned, and whose z faces are angled at the same angle as the palm of the hand, $\beta := 20°$. Otherwise, we instead specify a uniform minimum z height denoted z^- and no maximum height. The second case is designed so that if the planner predicts the cube will leave the palm, it prioritizes not dropping it and returning it back to the palm. See Fig. 3 for a visualization of these two cases.

The global origin of the system is located in the center of the interface between the hand mount and the bar of 80/20 to which it is affixed. The side length of the cube is $b := 0.07$. Let (p^c_x, p^c_y, p^c_z) denote the position coordinates of the center of the cube. The dimensions associated with the figure are specified in Table 3.

Cost Weights. The weights in (8) are $\lambda_{\mathrm{g}} = 1.0, \lambda_{\mathrm{p}} = 2.5$.

Time discretization. While (4) is expressed as an integral over the interval $[0, T]$, in practice we numerically compute it by discretizing the interval using a fixed time step Δt:

$$\int_0^T \ell\left(x(t), u(t)\right) dt \approx \sum_{j=0}^{H} \ell\Big(x(j\Delta t), u(j\Delta t)\Big) \cdot \Delta t, \tag{12}$$

where $H = T/\Delta t$.

Dim	Value
x^-	0.08
x^+	0.14
y^-	-0.02
y^+	0.02
z^-	$\begin{cases} \frac{b}{2\cos(\beta)} - p_x^c \cdot \tan(\beta), & \text{if } p_x^c \in [x^-, x^+],\ p_y^c \in [y^-, y^+] \\ -0.015, & \text{otherwise} \end{cases}$
z^+	$\begin{cases} z^- + 0.015, & \text{if } p_x^c \in [x^-, x^+],\ p_y^c \in [y^-, y^+] \\ +\infty, & \text{otherwise} \end{cases}$

Table 3: Dimensions of the set $\mathcal{S}$.

E Additional Details on Experiments

E.1 Hardware Setup and Experimental Details

For all experiments, we perform in-hand rotation of a 3D-printed cube with 7cm side lengths and a fixed-base LEAP hand [40] with palm angled downwards at 20° so that the cube slides off without intervention (see Fig. 1 and 2). We use a 128-thread Ryzen Threadripper Pro 5995wx CPU to plan rollouts in parallel. To capture images, we use three ZED Mini cameras with RGBD channels and perform keypoint estimation on 256x256 center-cropped images at VGA resolution. The estimator runs at about 90Hz, while the planner frequency fluctuates between 25-50Hz.

For our trials, we compare three planners: PS and CEM (the two sampling-based methods discussed in Sec. 2), as well as iLQR [41], a gradient-based method. PS and CEM use $N = 120$ rollouts while iLQR devotes 120 threads to parallel line search. CEM uses $M = 4$ elite samples. When tuning hyperparameters (such as cost weights), we prioritize robustness at the expense of rotation speed. For all experiments, we used identical costs, code, and hyperparameters for performing simulation rollouts, state estimation, and communicating with hardware. Unlike previous work [3, 4], we did not observe any significant degradation of our hardware stack (e.g., overheating) during testing.

E.2 Hardware Ablations

To understand the impact of key design choices in the DROP architecture, we conducted a series of single-variable ablations with the CEM planner on hardware (Table 1C).

Depth improves performance, but only marginally. We compared keypoint detection models trained on RGB versus RGBD images. While RGBD slightly improved rotation rates, it did not significantly outperform RGB, which still achieved 128 rotations, the longest sequence ever observed for DROP. Despite this noisy result, RGB's median rotations (28.5) were still slightly lower than RGBD's (30.5), and overall, the relative rotation rates suggest that depth provides a minor improvement in state estimation accuracy.

The corrector is key for performance. We tested DROP when ablating the corrector, passing raw smoother estimates $\tilde{q}$ directly to the planner. This significantly reduced performance, with mean rotations decreasing by 33%, median rotations by 60%, and rotation rate by 25%. Without the corrector, the planner often became trapped in local minima and long periods of inactivity (flat regions of rollouts in Fig. 5). This was caused by the exploitation of non-physical forces in rollouts arising from non-physical hand-cube interpenetration, leading to unrealistic predictions.

DROP is sensitive to the number of rollouts. We reduced the number of rollouts from 120 to 60 and elite samples from 4 to 3, resulting in a 20% decrease in mean rotation count and an over 25% reduction in rotation rate. This highlights the importance of variance reduction via sufficiently-high sample quantity in SPC, and suggesting that improving search efficiency could significantly boost performance.

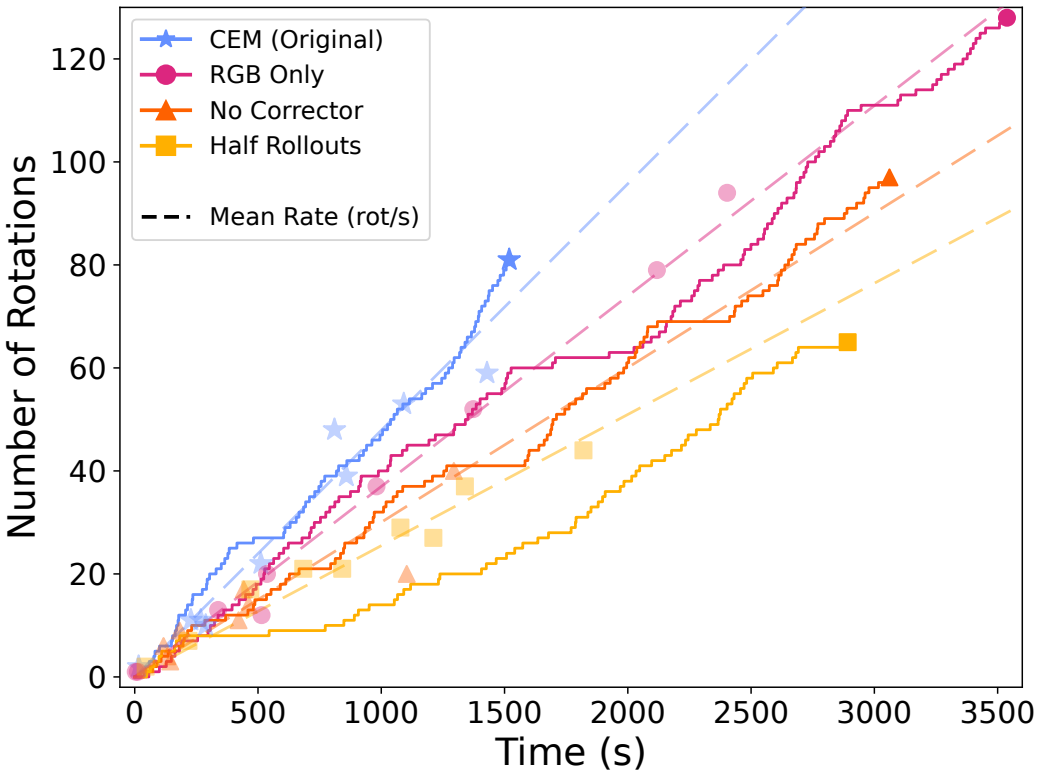

Figure 5: **CEM ablation rotation rates.** We use rotation rate as a proxy for planner robustness, as slower rates correspond to "stuck" plans or repeatedly failed moves. Markers are all rotations vs. times for CEM and all ablations. The dashed lines show the mean rotation rates: it is clear that all ablations decrease the rate, which justifies our design of the DROP architecture. The solid lines show individual rotations for each method's longest streak. The long, flat regions correspond to the planner getting "stuck" in local minima.

All ablations increased rotation rate variance. This consistent pattern demonstrates that depth measurements, the corrector, and sufficient rollout quantity all contribute significantly to the planner's reliability and consistency, which justifies the design of the DROP architecture.

E.3 Simulated Robustness Study

Lastly, we study DROP's robustness to model and estimation errors by conducting controlled trials in simulation, letting us isolate the planner from the estimation pipeline. We compared iLQR, PS, and CEM under various corrupted conditions, simulating system physics with a 2ms timestep while planner threads utilized a separate physics model with a 10ms timestep. Each configuration underwent five trials, ending upon cube drop, 80s timeout, or 150 rotations.

Specifically, we intentionally induce two types of errors that we believe contribute to real-world brittleness: (i) mis-tuning the planners' internal value of the hand K_p gains, and (ii) corrupting pose estimates from the simulation with a 0.1s lag and additive noise (simulated using a bounded random walk to mimic asymmetric state estimation error). When corrupting K_p, we study two cases: multiplying the true value by 1.25x and 1.5x, as the results were enlightening for comparing different planners. We also study the effect of the estimator and K_p errors together.

CEM is the most robust planner. Table 4 shows that CEM is the best planner under all error conditions. For example, while PS achieves a higher mean rotation count under perfect conditions than CEM, when K_p is mildly corrupted up to 1.25x, PS immediately achieves fewer mean rotations than CEM while suffering an over 2x decrease in rotation rate. At 1.5x, PS hardly rotates the cube at all, while CEM achieves 32.2 mean rotations, and even with the most aggressive errors, CEM was

Planner	Change	Mean Rot/s ↑	Mean Rots	Drops	Timeouts
iLQR	None	N/A	0 ± 0	3	2
PS	None	0.130	122 ± 54.8	1	0
	K_p x1.25	0.060	44.4 ± 26.4	1	4
	K_p x1.5	0.042	1.2 ± 1.17	0	5
	Est.	0.032	3.2 ± 1.72	5	0
	Est., K_p x1.25	0.048	3.4 ± 3.14	5	0
	Est., K_p x1.5	0.015	0.2 ± 0.40	3	2
CEM	None	0.222	95.4 ± 34.8	0	4
	K_p x1.25	0.148	52.8 ± 26.0	0	5
	K_p x1.5	0.100	32.2 ± 26.6	0	5
	Est.	0.120	46.8 ± 24.7	5	0
	Est., K_p x1.25	0.083	73.8 ± 26.4	4	1
	Est., K_p x1.5	0.058	24.8 ± 13.3	2	3

Table 4: **Simulated robustness tests.** We intentionally degrade planners to test their robustness by (i) tuning the hand proportional gain K_p too high, and (ii) corrupting the estimator with noise and lag (denoted "Est."). iLQR failed to achieve any rotations even with perfect information. We observe that PS degrades substantially more than CEM in the presence of model and estimation error, which suggests that CEM may transfer well to hardware.

able to achieve dozens of rotations. CEM's superiority can be attributed to its strategy of recomputing π_θ from multiple rollouts, in contrast to PS's single-rollout approach. This strategy appears to be key for robustness, providing a plausible explanation for CEM's markedly better performance in hardware.

Rot/s is a good proxy for robustness. Based on empirical observation, we find that low rotation rates are typically caused by the failure to execute precisely-planned motions or the inability of the planner to escape local minima, resulting in the cube being "stuck," which can be attributed to model or estimation error. CEM's superior speed in these simulations supports our assessments of its robustness on hardware.

Error types have distinct failure modes. While incorrect K_p values primarily resulted in timeouts, corrupted estimates typically caused cube drops. This suggests that perfect state estimates allow for safe "caging" even with poor actuation models, but estimation errors during precise maneuvers often cause drops, as the planner underestimates rollout risk.

F Dataset and Training of the Keypoint Predictor

Additional dataset details. We now further explain design decisions for the dataset used to train the vision model g_φ.

As described in Sec. C, the training images were sampled from frames of a video generated by simulating a random collection of objects (always including the cube) dropped from various positions and heights. These data were split into train and test datasets by first separating videos into train and test videos then by randomizing the order of all images from these videos. This ensured that very similar frames from the same video did not appear in both the train and test sets. Each video supplied 24 images.

In these videos, the cube's size was normalized such that its side length was 2.0m. Thus, when using the keypoint detector model downstream in conjunction with the smoother, the cube size must first be normalized.

Visual/material properties of the cube were randomized using `kubric` by uniform random sampling (see Table 5).

Property	Sampling Range
Roughness	[0.0, 0.3]
Specularity	[0.75, 1.0]
Metallic	[0.25, 0.75]
Index of Refraction	[1.0, 2.0]

Table 5: Cube material randomizations.

The camera pose was sampled such that it was always pointed at the origin, but its position was uniformly randomly located in some hemispherical shell with inner radius 7.0m, outer radius 9.0m, and z height exceeding 0.2m.

As described in Sec. C, images in the dataset where too few or too many pixels corresponded to the cube were removed, as this indicated that the cube was either too occluded or too close to provide an accurate keypoint estimate. Specifically, an image was included in the dataset only if the proportion of cube pixels was in the interval $[0.02, 0.7]$.

Lastly, we note that while the size of the training dataset is fairly large for such a specific task (about 686000 images), it is far fewer than number of images used to train cube pose estimators in other works (e.g., 5 million in [4] and we approximate 76.8 million in [3]). However, it is clear that an improved different approach will need to be used in order to generalize to different objects.

Image Augmentation Details. One of the key factors for robust keypoint prediction in the real world was the application of extensive image augmentations during training. The augmentations were randomly sampled and applied during training using a mix of implementations from the open-source image processing package `kornia` and custom augmentations described below. The `kornia` augmentations and parameters are described in Table 6. For detailed descriptions of the parameters, please see the `kornia` documentation. Any time the parameter `p` appears, it denotes the probability that the augmentation is applied.

Augmentation	Parameters

`RandomAffine`	`degrees: 90`
	`translate: (0.1, 0.1)`
	`scale: (0.9, 1.5)`
	`shear: 0.1`

`RandomErasing1`	`p: 0.5`
	`scale: (0.02, 0.1)`
	`ratio: (2.0, 3.0)`
	`same_on_batch: False`

`RandomErasing2`	`p: 0.5`
	`scale: (0.02, 0.05)`
	`ratio: (0.8, 1.2)`
	`same_on_batch: False`

`RandomPlanckianJitter`	`mode: blackbody`

`ColorJiggle`	`brightness: 0.2`
	`contrast: 0.4`
	`saturation: 0.4`
	`hue: 0.025`

`RandomGaussianBlur`	`kernel_size: (5, 5)`
	`sigma: (3.0, 8.0)`
	`p: 0.5`

`RandomPlasmaShadow`	All defaults

Table 6: All RGB image `kornia` augmentations used during training. Augmentation parameters are defaults if unspecified.

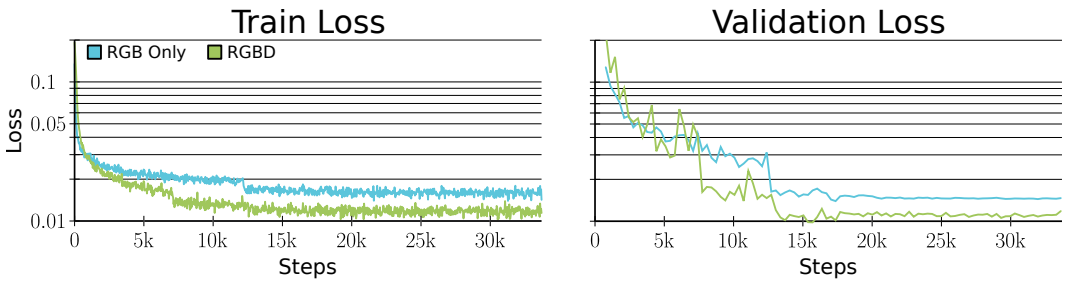

Figure 6: Training and validation loss curves for the RGBD and RGB-only vision models. Note that the curves are log scale.

We implemented custom augmentations that applied only to depth images, as well as a custom augmentation for transplanting random backgrounds onto training images. We describe these now and summarize the associated parameters in Table 7.

For the depth readings, we (i) uniformly randomly sample a per-image bias (`DepthBias`), (ii) add Gaussian noise (`DepthGaussianNoise`), and (iii) uniformly randomly sample near and far planes centered about some mean value, where everything too close or far is set to 0.0 (`DepthPlane`).

Lastly, we implemented a special augmentation called `CustomTransplantation` (not to be confused with the `RandomTransplantation` augmentation in `kornia`), which requires a batch of RGBD images as well as segmentation masks for the cube. With some probability, each image in the batch (the acceptor) has all of its non-cube pixels replaced by pixels from another image in the batch (the donor) using the following procedure. First, all non-cube pixels in the acceptor are identified, which initializes a background mask. Second, all pixels in the donor that are closer to the camera than the corresponding pixels in the acceptor are added to the background mask. Third, the pixels in the donor mask corresponding to the cube in the donor are removed from the mask (to prevent there from being two cubes in a single image). Fourth, the background mask selects pixels from the donor and replaces the corresponding pixels in the acceptor. Finally, if the resulting transplanted image results yields an image that has too large or small of a ratio of visible cube pixels, the transplantation is not applied. This transplantation method allows backgrounds from donors to further obscure the cube in acceptors in random ways, which helps improve robustness.

Augmentation	Parameters
`DepthBias`	`bias_range: (-0.02, 0.02)` `p: 0.5`
`DepthGaussianNoise`	`stdev: 0.005`

`DepthPlane`	`near_mean: 0.1`
	`near_range: (-0.05, 0.05)`
	`p_near: 0.5`
	`far_mean: 0.5`
	`far_range: (-0.05, 0.05)`
	`p_far: 0.5`

`CustomTransplantation`	`p: 0.5`
	`ratio_lb: 0.02`
	`ratio_ub: 0.7`

Table 7: Parameters for our custom augmentations.

Training Hyperparameters. Training hyperparameters are described in Table 8. We trained the model using a machine with 8 H100 GPUs for about 8 hours, though we remark that using this many GPUs is not required.

Training and Validation Curves. We show the training and validation curves for the RGBD model as well as the RGB-only model used in the ablation study from Sec. E.2 in Fig. 6. Overall, the

Hyperparameter	Value
batch_size	256
learning_rate (initial)	1e-3
epochs	100
num_workers	4
AMP	True
Loss Function	MSE
Optimizer	AdamW
Scheduler	ReduceLROnPlateau patience: 5 factor: 0.25 min_lr: 1e-6 grad_scaler: True

Table 8: Training Hyperparameters.

RGBD model seems to perform slightly better, but not by a large margin. Note that the figure is in log scale.

G Smoother Details

This section provides a cursory overview of factor graphs, explains the setup of the graph used in DROP's estimation problem, and describes implementation details and hyperparameters of the smoother.

A primer on factor graphs. Factor graphs are a type of probabilistic graphical model that models the relationships between unknown random variables via *factors*, which can be interpreted as (unnormalized) likelihood functions of subsets of all of the unknowns parameterized by measurements, which themselves are functions of the same unknowns. The factor graph defines a factorization of some global likelihood function over all unknowns, which gives us a computationally-convenient framework for performing *maximum a posteriori* (MAP) inference to recover an estimate of the unknowns. For further explanation, we refer the reader to [**?**].

Let X denote the total set of all unknowns and X_l denote some indexed subset of X. Then, we can represent the factors formally as

$$\phi(X) = \prod_l \phi_l(X_l), \tag{13}$$

which models the independence relationships between the unknown variables of interest. Now, let measurements be modeled $z_l = h_l(X_l)$, where h_l is some measurement model. Then, with a Gaussian noise model and the assumption that the factors take the form

$$\phi_l(X_l) \propto \exp\left\{-\frac{1}{2}\left\|h_l(X_l) - z_l\right\|^2_{\Sigma_l}\right\}, \tag{14}$$

the MAP solution for the unknown variables is equivalent to the following nonlinear least squares problem:

$$X^{\text{MAP}} = \arg\min_X \sum_l \left\|h_l(X_l) - z_l\right\|^2_{\Sigma_l}. \tag{15}$$

In practice, the MAP inference problem is solved by numerical methods like the Gauss-Newton or Levenberg-Marquardt algorithms, which converge to some local minimum by solving successive linearizations of (15).

In practice, we also used a *robust Huber error model* to reduce sensitivity to outlier measurements (see this GTSAM blog post for more information: gtsam.org/2019/09/20/robust-noise-model.html).

Incremental smoothing. We are interested in the setting where we receive a stream of incremental information and we seek to update the MAP estimate over time. In particular, we consider a canonical

graphical model of a dynamical system with two types of factors: *dynamics* factors that model the (Markovian) temporal transitions between states ($\phi_t^{\text{dyn}}(X_{t+1}, X_t)$), and *measurement* factors that model the likelihood of observations on those states ($\phi_t^{\text{meas}}(X_t; z_t)$).

Because the graph would rapidly grow in size as time elapses, when incrementally smoothing, it is common to *marginalize* out the effect of older unknowns to retain their information content while removing them from the graph (see [**?** , Sec. 5.3]). This way, the number of variables remains fixed and the estimation problem stays tractable.

This scheme gives rise to *fixed-lag smoothing*, where some lookback window specifies the number of states in the past to maintain in the graph at each time step. The case where the lookback is 1 corresponds to the standard *Kalman filter*.

The cube pose estimation factor graph. In DROP, we seek to estimate the cube poses (and velocities) over time. For computational speed, we do not model the full dynamics of the cube-hand system (which gives rise to the need for the corrector later). In particular, the stiff contact dynamics would introduce substantial numerical challenges when conducting successive linearizations to solve (15).

Instead, we use a *constant velocity model* to approximate the cube dynamics. Because the linear and angular velocity of the cube is typically small when supported by the palm, this simple model (accompanied by a sufficiently tuned mistrust of it) provides a coarse but sufficiently-accurate model of the cube's motion.

For a given camera with a known global pose in conjunction with a pinhole camera model, the measurement model computes the expected keypoint locations in the camera's image frame (in pixel coordinates). The "true" measurements come from the keypoint predictor network g_φ.

Sketch of the keypoint projection factor. The keypoint factor (one for each keypoint, indexing suppressed for clarity) for a camera has the form

$$\phi_t^{\text{meas}}(q_t^c; \nu^{\text{cam}}, p_{\text{kp}}^{\text{pix}}, p_{\text{kp}}^c, p^{\text{cam}}, r^{\text{cam}}), \tag{16}$$

where q_t^c is the pose of the cube at time t, ν^{cam} is the camera's known intrinsics, $p_{\text{kp}}^{\text{pix}} \in \mathbb{R}^2$ is the measured keypoint locations in pixel coordinates from the predictor g_φ, $p_{\text{kp}}^c \in \mathbb{R}^3$ is the location of the associated keypoint in the cube's local frame, and $(p^{\text{cam}}, r^{\text{cam}}) \in SE(3)$ is the known fixed pose of the camera in the world frame.

Let the function $\text{proj} : \mathbb{R}^3 \to \mathbb{R}^2$ project a spatial point expressed in the camera frame to a coordinate in pixel space, which is implemented in GTSAM [38]. The measurement residual is then computed as follows:

$$p_{\text{kp}}^{\text{pix}} - \text{proj}(p_{\text{kp}}^c; \nu^{\text{cam}}, p^{\text{cam}}, r^{\text{cam}}), \tag{17}$$

where the Jacobians associated with frame transforms and the projection function are also computed by GTSAM. For the exact implementation details, please see our open-source implementation [37].

Smoother parameters and other details. We summarize all parameters in Table 9. All quaternions are reported in wxyz order. Noise parameters are given by standard deviations σ corresponding to diagonal components of the noise model covariance matrices. Rotational noise is represented by Gaussian noise in the tangent space. Huber regularization is applied identically to all noise models.

H Corrector Implementation

As describe in Sec. C, the corrector applies a virtual corrective wrench to its internal estimate of the cube state as shown in (7). The corrector gain matrices have 6 diagonal entries corresponding to the virtual forces and torques applied to the cube. We use the values

$$\begin{aligned} C_P &= \text{diag}([1000, 1000, 1000, 3, 3, 3]), \\ C_D &= \text{diag}([1, 1, 1, 0.001, 0.001, 0.001]). \end{aligned} \tag{18}$$

Parameter	Value
Cube Pos Prior	$p = [0.1, 0.0, 0.0]$ $r = [1.0, 0.0, 0.0, 0.0]$ $\sigma_p = [0.5, 0.5, 0.5]$ $\sigma_r = [1.0, 1.0, 1.0]$
Cube Vel Prior	$v = [0.0, 0.0, 0.0]$ $\omega = [0.0, 0.0, 0.0]$ $\sigma_v = [0.01, 0.01, 0.01]$ $\sigma_\omega = [0.2, 0.2, 0.2]$
Dynamics Pos Noise	$\sigma_p = [0.01, 0.01, 0.01]$ $\sigma_r = [0.2, 0.2, 0.2]$
Dynamics Vel Noise	$\sigma_v = [0.01, 0.01, 0.01]$ $\sigma_\omega = [0.2, 0.2, 0.2]$
Measurement Noise (in pixels)	$\sigma_z = [3.0, 3.0]$
Meas. Robustness Parameter k_{huber}	1.345
Lookback Window	1

Table 9: Smoother parameters.

The extra gravitational corrective force described in Sec. C is simply an extra 10N added along the $-z$ axis of the virtual forces applied to the cube.

Additionally, there are a few parameters of the corrector dynamics $\hat{f}$ that differ from the planner's internal model f, which we show in Table 10.

Parameter	Value
Timestep	0.04s
LEAP Hand k_p	3.0
`solimp`	[0.999, 0.999, 0.001, 0.0001, 1]
`solref`	[0.0001, 1]

Table 10: Parameters of the corrector's internal model $\hat{f}$ that differ from the planner's internal model f.

I Miscellaneous Hardware Implementation Details

While the stack described in Sec. 2 is fairly simple, there are a few miscellaneous details that affect performance.

LEAP hand gains. The scale of the gains in the simulated model and on hardware are quite different. While in simulation, the planner's LEAP hand gains are $k_p = 1.0$ and $k_v = 0.01$, on hardware, we use $k_p = 75$ and $k_v = 25$. In fact, the hardware gain values are already quite low compared to the values recommended in [40]. This was intentional; by lowering the gains, we lowered the amount of energy imparted on the cube, and allowed the controller to manipulate the cube with a higher degree of control.

The physical cube. The cube itself is made of low-density 3D-printed PLA, weighing 0.108kg. The faces of the cube are simply printed out on regular printer paper and taped onto the cube using reflective, low-friction packing tape. We remark that over time, the frictional properties of the cube may slightly change. Our reported experiments were run using a cube that was used for about 1 week prior, and anecdotally, the friction increased slightly over this period, which helped prevent the cube from slipping out of the hand. In the weeks prior to our final experimental trials, older versions of the cube also exhibited peeling tape, torn faces/edges, and other effects that substantially increased the friction of the cube. For the most repeatable results, we would recommend re-taping a cube from scratch every few weeks.

Manual calibration of camera poses. Before running experiments, we found it important to perform some manual adjustments of each camera's ground-truth pose with respect to the world frame. To

perform the calibration, we streamed the estimated cube pose from the smoother and projected the associated analytical keypoint locations back onto each camera's image frame using the keypoint factors derived in App. G. By adjusting the camera position, we were able to manually align the projected keypoints with the corners of the cube.